Single-cell imaging of the lytic phage life cycle in bacteria

Charlie Wedd[1], Temur Yunusov[2], Aaron Smith[2], Ruizhe Li[1], Georgeos Hardo[1], Michael Hunter[2], Racha Majed[2], Diana Fusco[2]*, Somenath Bakshi[1]*

[1]Department of Engineering, University of Cambridge, Trumpington Street, Cambridge, CB2 1PZ, UK.
[2]Department of Physics, University of Cambridge, JJ Thomson Avenue, Cambridge, CB3 0HE, UK.

*Corresponding author(s). E-mail(s): df390@cam.ac.uk; somenath.bakshi@eng.cam.ac.uk

Abstract

When a lytic bacteriophage infects a bacterial cell, it commandeers the cell's resources to replicate, ultimately causing cell lysis and the release of new virions. As phages function as obligate parasites, each stage of the infection process depends on the physiological parameters of the host cell. Given the inherent variability of bacterial physiology, we ask how the phage infection dynamic reflects such heterogeneity.

Here, we introduce an imaging assay for investigating the kinetics of individual infection steps by a single T7 phage on a single bacterium. The high-throughput, time-resolved nature of the assay allows us to monitor the infection progression simultaneously in multiple cells, revealing substantial heterogeneity in each step and correlations between the dynamics of infection steps and physiological properties of the infected cell. Simulations of competing phage populations with distinct lysis time distributions indicate that this heterogeneity can have considerable impact on phage fitness, recognising variability in infection kinetics as a potential evolutionary driver of phage-bacteria interactions.

Key words:

T7 phage, Single-cell, Microfluidics, High-throughput microscopy, Phage genome injection, Phage infection, Host takeover, Cell lysis, Phage evolution

Introduction

Bacteriophages, viruses that infect bacteria, play pivotal roles in shaping bacterial communities in nature and hold significant promise in medicine and biotechnology as biocontrol agents[1,2]. Among them, lytic bacteriophages stand out for their potential in combating antibiotic-resistant infections[2]. As these viruses rely on the host molecular

machinery and precursors to proliferate, the infection-to-lysis process intricately depends on the physiological characteristics of the target cell: for instance, factors such as lipopolysaccharide (LPS) composition and receptor density influence the adsorption rate[3]; the resources and machinery of the host cell affect the rate of virion replication[4,5] and the production of lytic agents necessary for cell lysis. Recent single-cell studies have unveiled significant physiological variability among genetically identical bacterial cells, raising questions about how this diversity impacts the kinetics of phage infection and how the variability in infection kinetics, in turn, influences the overall effectiveness of phages in eliminating their target bacteria at a population level[6].

The vast majority of current methods used to study the kinetics of phage infections steps in bacteria rely on bulk culture approaches and omics analysis[7–9], which lack the necessary single-cell resolution to analyse cell-to-cell heterogeneity, or on cryo-EM imaging for high-resolution investigation of structural aspects, which lacks time-resolved information to monitor the progress of individual infection steps and their interrelations[10,11]. Recent single-cell studies have revealed unprecedented insights into the mechanisms underlying the lytic-lysogenic switch of temperate phages[12]. However, few studies have attempted to analyse lytic phage infection at single-cell level and to understand how the physiological diversity of host cells influences the infection cycle[13,14]. To achieve this, a method is needed that can: (i) precisely track each stage of infection initiated by a single phage targeting a solitary living bacterium in a time-resolved fashion, (ii) maintain a spatiotemporally homogeneous environment to isolate the impact of intrinsic variations in host cell physiology on infection parameters, and (iii) be sufficiently high throughput for quantifying the detailed distribution across these target bacterial cells.

Here, we present an innovative approach tailored to address these challenges. Our method harnesses a microfluidic platform engineered to maintain isolated populations of target cells under uniform growth conditions, to enable the tracking of infection dynamics as individual cells become infected and lysed by individual phages. Using high-speed scanning time-resolved microscopy[15], and a combination of fluorescent markers on the model system of phage T7, we are able to follow individual infection events from phage adsorption to cell lysis on individual cells of *Escherichia coli*. Altogether, the method provides the first quantification of the timing and variability in the kinetics of lytic phage infection steps. Moreover, employing this method allows us to correlate the observed fluctuations in infection parameters with the physiological parameters of the host, thereby elucidating the source of such variations.

Analysis of these comprehensive datasets has yielded unprecedented insights into the temporal dynamics and variability of each infection stage, revealing their detailed distributions, interrelationships, and broader implications in terms of selective pressure on phage populations. Results from our simulations show that the details of the distribution of these kinetic parameters are crucial in determining the competitive fitness of a lytic phage, suggesting that variability in the phage life history parameters could constitute an evolutionary trait that is currently under-explored. Looking forward, we anticipate that our method will offer the opportunity to quantify the distribution of infection parameters, revealing an understanding of phage-bacteria interactions and their evolution previously unattainable.

Results

Single cell imaging of the T7 phage infection cycle

To identify and monitor the timing of the different steps in the T7 life cycle using fluorescence microscopy, we introduced two fluorescent labels in the phage (Fig. 1a). First, we modified the wild-type T7 genome to include a fluorescent reporter of capsid gene expression (gp10A-B, Methods, Supplementary note 1). The capsid genes are among the most highly expressed T7 genes[16], making them an excellent target to obtain a strong fluorescent signal for phage transcription. mVenus NB, a yellow fluorescent protein (YFP) with a very fast maturation time (4 min)[17], was selected as suitable fluorescent reporter given the short phage life cycle (15-20 min)[18]. This modified T7 phage (referred to as T7*) was then stained with a DNA binding dye, SYTOX Orange (Fig. 1a, Methods, Supplementary note 2), to visualise phage adsorption to the host cell (t_0) and subsequent genome injection. SYTOX Orange is spectrally compatible with the YFP reporter, has been previously used for labelling lambda phage genome[19] and does not affect cell growth[20].

Individual phage infection cycles in single bacterial cells (*E. coli* MG1655 7740 ΔmotA) were monitored using a modified version of the 'mother machine' microfluidic device[21]. In this device, cells are cultivated in linear colonies within narrow (1.4 μm wide) trenches, receiving nutrients diffusively from the media flowing through the orthogonal flow channel (Fig. 1b). In contrast to the regular mother machine design[22], the narrow trenches are flanked by shallow side trenches that facilitate the diffusion of both nutrients and phage along the length of the trench[21]. We found that the presence of side trenches is essential for phages to infect cells deeper in the trench, so that infection events can be monitored over time all the way to lysis before the corresponding infected cell is pushed out of the trench by the replicating cells above (Supplementary note 3). As individual lineages are isolated in their own trenches and the media continuously flows throughout the experiment, the device maintains cells in a spatiotemporally uniform environment. This uniformity is key to minimise potential sources of heterogeneity arising from a variable environment and truly quantify the stochasticity of individual steps in the infection process across a bacterial population experiencing identical external conditions. Additionally, as we operate at very low multiplicity of infection, we can ensure that the first lysis events in each trench are truly originating from the infection of one bacterium by one single phage, as evidenced by the rare occurrences of such events (Supplementary movie 1).

The cells are loaded into the device and grown in LB Miller with pluronic for a minimum of three hours to allow them to reach a steady-state exponential growth phase. Subsequently, the media is switched to media with added phage (Methods). High-speed time-resolved scanning microscopy[15] was used to collect multichannel data at high time-resolution (2 frames min^{-1}) during the infection events (Supplementary movie 2) and processed using a machine-learning model trained with synthetic micrographs[23] (Methods, Supplementary note 4), to quantify cell physiology and infection markers over time. Individual infected cells were tracked across frames using a custom-designed lineage-tracking algorithm, which accommodates the disappearance of a subset of cells due to phage-induced lysis (Supplementary note 5). An example of a resultant multichannel kymograph of a single infection event is shown in Fig. 1c and its corresponding time-series data in Fig. 1d. In the orange channel, the adsorption of the

SYTOX Orange stained phage to a cell is seen as an orange dot (t_0), which fades and disappears over time as the genome is injected (t_1). In the yellow channel, the YFP signal of the capsid production reporter can be seen increasing in intensity (t_3) after genome injection is completed and up to cell lysis. The phase contrast channel shows cell growth up until a point, post-phage-adsorption, when the growth in length stops abruptly (t_2), and the cell eventually lyses (t_5). In the following sections, we analyse the heterogeneity of each of these steps across different infection events.

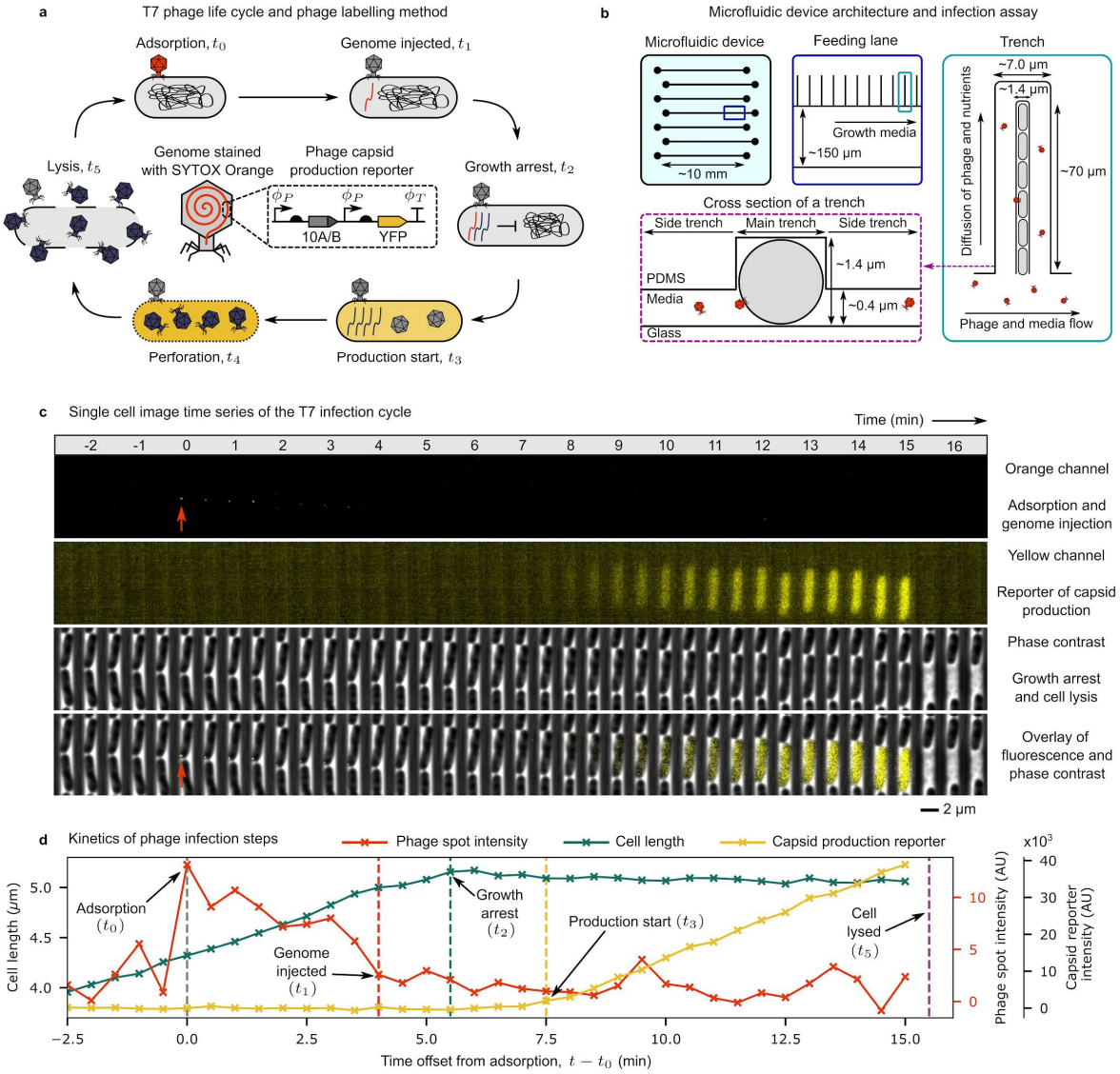

Fig. 1: An assay for imaging the T7 phage infection cycle at the single-cell level
a. An overview of six key time points in the T7 life cycle, which we use throughout the study to quantify the kinetics of infection steps in the phage life cycle. The DNA staining method and genomic location of the capsid production reporter are indicated in the centre of the loop. **b.** A description of the microfluidic device and infection assay used in this study. **c.** Kymographs showing a T7* phage (indicated by the red arrow) infecting a single bacterial cell. The orange channel image has been bandpass filtered to remove bleedthrough from the YFP capsid production reporter (Supplementary note 6). **d.** Time series data corresponding to the phage infection images presented in (**c**) demonstrate the typical progression of signals during T7*

infection. With the exception of perforation, which happens very close to lysis, all time points from Fig. 1a are labelled on the time series.

Genome injection kinetics show two distinct entry modalities

The molecular mechanisms that lead to T7 genome entry have been extensively studied[24–27] and result in a three-step process: (i) up to the first 850 base-pairs[28] enter the cell as the phage tail penetrates the cell wall and membrane, (ii) the host RNA polymerase (RNAP) recognises a series of binding sites on the genome and translocates it while transcribing the early genes, including the T7 RNAP, (iii) once expressed, the T7 RNAP takes over the process and pulls in the remaining 85% of the genome.

Studies in bulk cultures have shown that the whole process takes approximately 4 minutes on average[28,29], however, the variability of its dynamics within a population is unknown. In our setup, we can track such dynamics across multiple infection events, by quantifying the fluorescence signal coming from the labelled phage DNA over time (Fig. 2, Methods, Supplementary note 7). When the phage binds to a cell, a bright spot suddenly appears in the orange channel due to the immobilisation of the phage upon adsorption (Fig. 2c). The fluorescence intensity of the spot then decreases over time as the genome gradually leaves the viral capsid and enters the cell (Supplementary movie 3).

Across multiple adsorption events, we observed significant heterogeneity in the progression of genome injection (Fig. 2d-e). The intensity trends reveal two broad classes of entry dynamics. In one, the injection progresses steadily to completion at an approximate rate of 4 kbps min^{-1} (Supplementary note 8). In the other, the entry proceeds similarly up to approximately 1.5 min, but then a sudden transition occurs in which the rest of the genome quickly enters the cell. These results suggest two potential modes of entry. The first class of trajectories would be consistent with the host RNAP being responsible for translocating the whole phage genome into the cell (*E. coli* RNAP's transcription velocity is between 1.2 and 5.4 kbps min^{-1})[30]. The second class aligns with the established three-step genome entry process, in which the first 6 kbps of the phage genome are translocated by the host RNAP and the rest by the much faster T7 RNAP. The distribution of the injection time duration (Fig. 2e) displays a mean duration time of 4.9 min, consistent with previous bulk experiments, with a large variability across infection events (coefficient of variation (CV) = 74%, n = 31). This large variability could be explained by the observed bimodality of the process in which approximately one third of the injection events belong to the first class, and two thirds to the second.

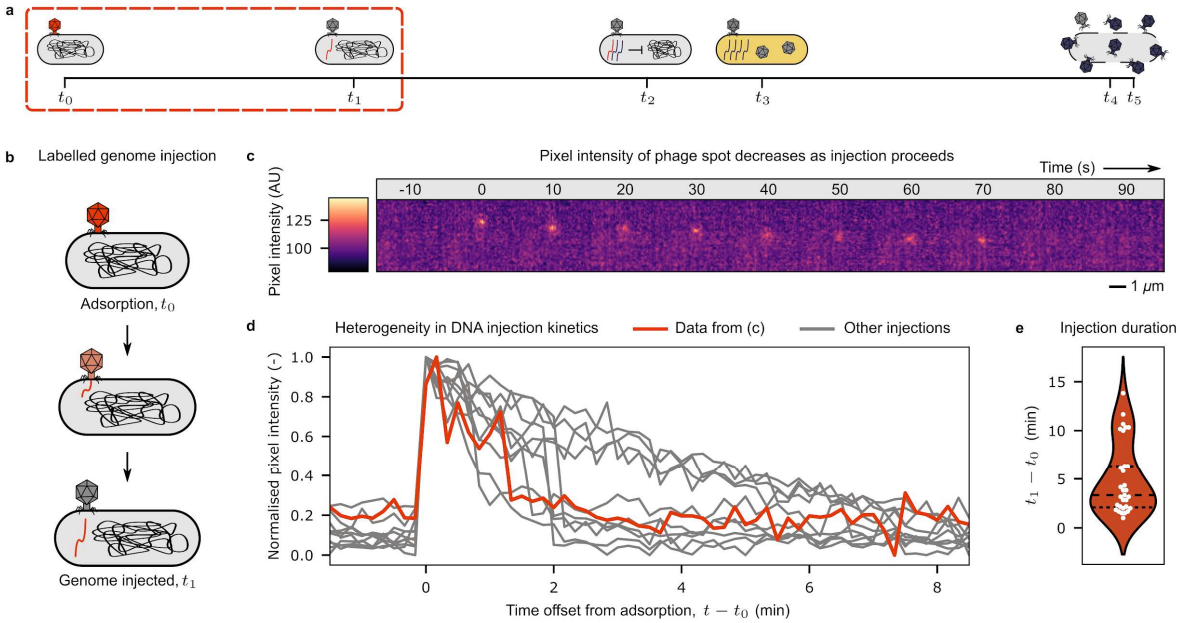

Fig. 2: Heterogeneity in phage genome injection kinetics
a. A timeline showing the temporal location of genome injection in the T7 life cycle. **b.** A schematic of T7 genome injection. **c.** A kymograph of genome injection shown as a heat map. The phage spot moves vertically downwards in sequential frames due to cell growth. **d.** A comparison of phage spot intensities over time for several genome injection events. Signals have been background corrected and normalised. The injection shown in (**c**) is displayed in orange and examples of ten other injections are displayed in grey. **e.** A violin plot showing the distribution of genome injection durations (t_0 to t_1). The central dashed line represents the median and the outer dashed lines the first and third quartiles. The mean injection duration is 4.9 min (n = 31, CV = 74%).

Kinetics of host cell shutdown and viral takeover are remarkably consistent across infection events

The T7 early (class I) genes, transcribed at the beginning of the infection process by the host RNAP, are responsible for the shutdown of the host cell, including the inhibition of cell wall synthesis[31,32]. We therefore expect cell growth arrest to be among the first signs that phage proteins are being produced. Our fluorescent transcriptional reporter for the capsid proteins, in addition, pinpoints the onset of expression of late (class III) genes from the phage genome. Together, these two markers (growth arrest and capsid expression reporter) allow us to analyse the kinetics and variability in phage protein production during the infection process (Fig. 3a).

A representative time series from a single infection event is illustrated in Fig. 3b. The green line depicts cell length, $L(t)$, where the abrupt periodic drops prior to infection correspond to cell division events. The instantaneous growth rate for each cell, λ, is calculated from the local slope of the $ln\,(L(t))$ time series (Fig. 3c, Supplementary note 9). The precise moment of growth arrest (t_2) is determined when the instantaneous growth rate falls below a given threshold (Supplementary note 9). Soon after growth arrest is detected, we observe the level of capsid expression ($I(t)$, yellow line) to increase rapidly until lysis occurs (Fig. 3b).

Growth arrest dynamics are found to be remarkably robust across different infection events (Fig. 3c). Cells transition from pre-infection growth rates to complete cessation within 3-4 min and in a consistent fashion, independently of their size or position in the cell-cycle. By contrast, expression of the capsid reporter displays considerable variability (Fig. 3d), with the maximum intensity of the reporter, I_{max}, varying by almost an order of magnitude across infection events. We found the variability in I_{max} to be strongly correlated with the size of the growth arrested cell (L_{GA}) (Fig. 3d, right). Larger production rates in larger cells would be consistent with the presence of more ribosomes, which is likely the limiting factor in phage protein production. We investigate this in the next section.

In five of the 23 example infections presented in Fig. 3d, the YFP intensity sharply decreases in the final observation before lysis (highlighted in green, Fig. 3d). This decline in signal coincides with the perforation of the cell envelope (t_4, detailed in Fig. 5 and Supplementary note 10).

Unlike the genome injection process discussed earlier (t_0 to t_1), the time intervals between growth arrest and subsequent lysis (t_2 to t_5) and between start of capsid production and lysis (t_3 to t_5) are narrowly distributed (respectively, CV of 15% and 17%, Fig. 3e), with the latter delayed on average by 1.9 min compared to the first. We note here that the folding and maturation of the reporter proteins can take minutes, implying that actual expression of the capsid genes might start at the same time, if not earlier than the growth halt of the host cell. Taken together, these results suggest that once the phage has taken control over the cell, the timing of events proceeds almost deterministically.

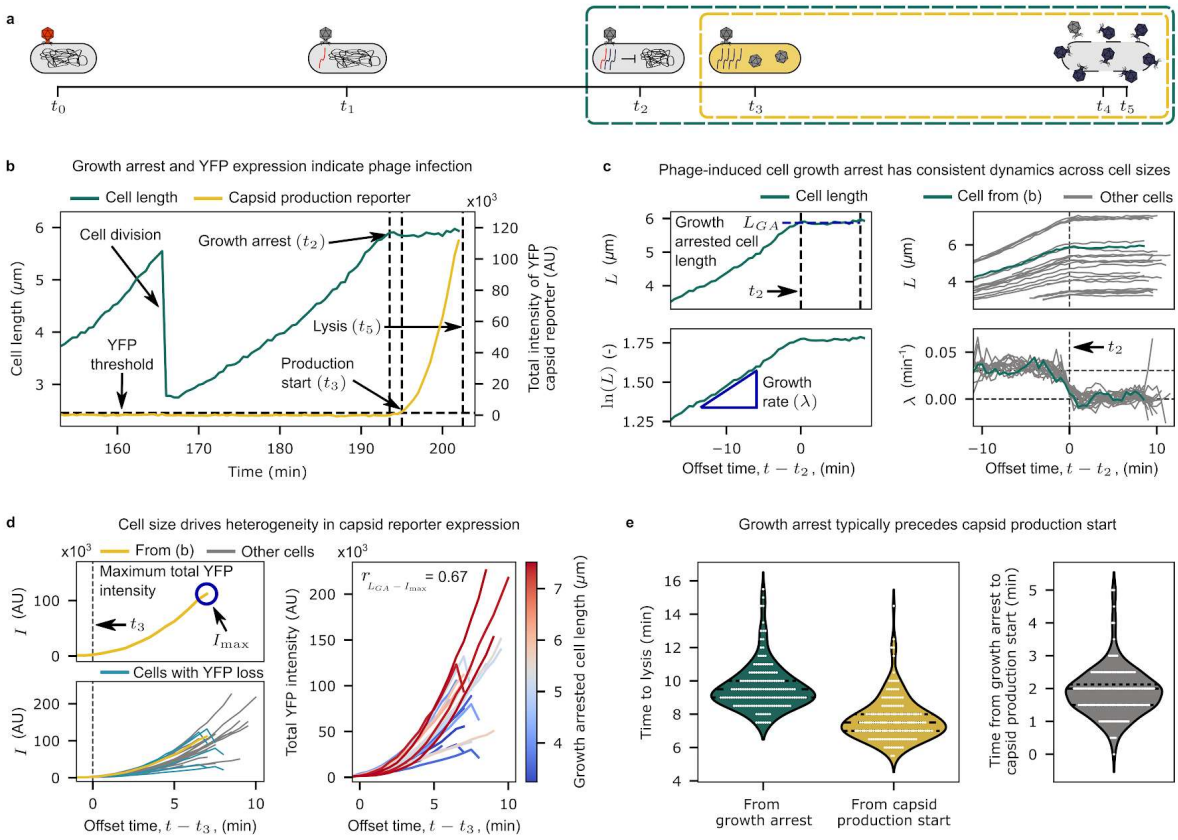

Fig. 3: Kinetics of host shutdown and phage gene expression

a. A timeline showing the temporal location of growth arrest and capsid production start in the T7 life cycle. **b.** Example time series data showing representative cell length and capsid reporter expression data of a cell which becomes infected. Three time points, the growth arrest (t_2), capsid production start (t_3) and lysis (t_5), are indicated. The threshold intensity used to define production start is also indicated. **c.** We use the growth arrested cell length as a measure of cell size after host takeover (left, top panel). The cell growth rate is calculated as the instantaneous slope of the natural log-transformed cell length (left, bottom panel). Comparison of the cell length (right, top panel) and growth rate (right, bottom panel) between the cell in panel (**b**) (green lines) and 22 other infected cells (grey lines). The growth arrest kinetic is highly consistent between cells. **d.** Capsid reporter production is highly variable between different infection events. We use total YFP intensity summed over the cell, I, as a measure of capsid reporter production, and hence the maximum total YFP intensity, I_{max}, (left, top panel) as a proxy for the total number of capsid proteins produced in a cell. Example data from 23 infection events (left, bottom panel) shows the variability in capsid reporter production kinetics, comparing the example from panel (**b**) (yellow line) to other events (grey lines). Five events are highlighted in green; these cells show a sharp drop in YFP signal in the final observation before lysis due to the perforation of the cell envelope (see Supplementary note 10). The variability in production kinetics is linked to differences in cell size (right). The lines are coloured by the growth arrested cell length of each cell and the maximum total YFP intensity is positively correlated with the growth arrested cell length (r = 0.67). **e.** Growth arrest typically precedes production start by a mean time delay of 1.9 min. The violin plots show kernel density estimates of the timings from growth arrest (green) and production start (yellow) to lysis, along with the timings between growth arrest and production start (grey). The central

dashed line represents the median and the outer dashed lines the first and third quartiles. The mean time from growth arrest to lysis (t_2 to t_5) is 9.6 min (n = 166, CV = 15%). The mean time from production start to lysis (t_3 to t_5) is 7.7 min (n = 160, CV = 17%). The mean time from growth arrest to production start (t_2 to t_3) is 1.9 min (n = 160, CV = 39%).

Phage protein production kinetics are strongly coupled with the physiological variability of the host

The observed high variability in protein production, despite the remarkable robustness of timing of events, hints to other sources of heterogeneity beyond production time. To understand the source of this heterogeneity and its correlation with the cell size at the moment of growth arrest, L_{GA} (Fig. 3d), we developed a mathematical model that takes into account viral genome replication, transcription, and translation (Fig. 4a, details in Supplementary note 11). In brief, the model assumes that the phage genome replication is autocatalytic, and the genome replicates exponentially with a rate λ_1. If the number of genome copies and not T7 RNAP is the limiting factor in transcription, this leads to an exponentially growing amount of mRNA encoding YFP. The translation rate, and thus YFP production, depends on the available number of mRNA copies, m, and the number of ribosomes present in the cell according to a simple Hill equation (Fig. 4a, Supplementary note 11). The maximum translation rate, λ_2, is then a proxy for the total number of ribosomes in the cell.

The dynamics of YFP can be solved analytically, providing simple functional forms for $dYFP/dt$ as a function of YFP and of YFP as a function of time:

$$dYFP/dt = \lambda_2[1 - exp(-\lambda_1/\lambda_2 YFP)], \quad (1)$$

$$YFP = \lambda_2/\lambda_1 log\{1 + \{exp[\lambda_1(t - t_3 *)] - 1\}/K_0\}, \quad (2)$$

where $K_0 = K/m_0$ (Fig. 4a and Supplementary note 11).
These allow us to estimate the model parameters from the experimental fluorescence intensity time series (Fig. 4a, Supplementary note 11). By fitting each cell's time series, we can extract values for λ_1, λ_2 (from eq. 1), and the time, $t_3 *$ (from eq. 2) at which protein production starts (Fig. 4b). We find that the maximum translation rate, λ_2, strongly correlates with maximum YFP values, pointing at the number of ribosomes in the infected cell as the key variable controlling phage protein production (Fig. 4b). By contrast, production time, defined as $t_5 - t_3 *$, shows only a weak correlation with maximum YFP, in line with the idea that the major source of variability in phage protein production lies in the number of ribosomes of the infected cell and, therefore, the cell's physiological state at the time of viral takeover, and not the latent period of infection, as previously thought[33–35].

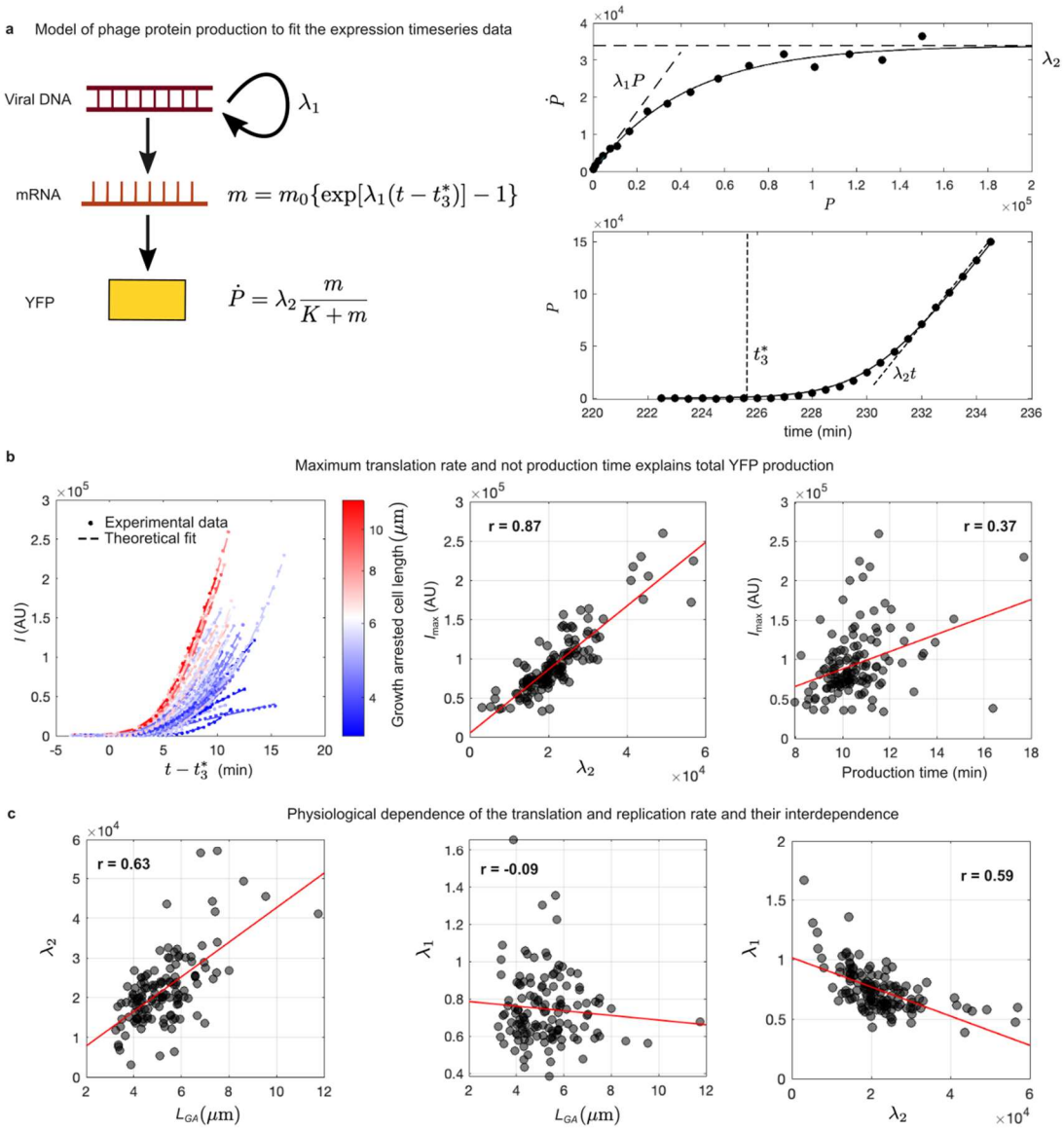

Fig. 4: Maximum translation capacity explains phage protein production
a. Schematic diagram of the mathematical model for phage protein production from viral genome duplication, through gene transcription to protein translation. The two analytical functions, dP/dt as a function of P (eq. 1) and P as a function of time (eq. 2) are sequentially used to fit the experimental data and determine λ_1, λ_2, and production start time, $t_3 *$. **b.** Time-series data of YFP expression are shifted to align production start time ($t_3 *$), with traces coloured according to cell length at growth arrest. The maximum YFP signal observed, I_{max}, strongly correlates with the inferred maximum translation rate λ_2, and only moderately with inferred production time ($t_3 *$ to t_5). **c.** Maximum translation rate correlates with cell length at growth arrest (L_{GA}), linking cell physiology with this parameter. By contrast, phage genome duplication rate, λ_1, shows no correlation with host cell features (Supplementary note 11). Intriguingly, λ_1 and λ_2 show a negative correlation.

Unsurprisingly, we find that λ_2 positively correlates with cell size at the point of growth arrest (Fig. 4c), which explains the empirical correlation between maximum YFP and cell size in the

experimental data (Fig. 3d). Importantly, our YFP marker was designed to track capsid protein expression and, as such, is our best proxy for the number of viral capsids produced by the infected cell, i.e., the burst size. Our results therefore suggest that burst size could, in principle, vary by almost one order of magnitude even in perfectly homogeneous conditions, simply because of physiological differences across infected cells.

Beyond maximum YFP production, the model results reveal some additional intriguing observations. The lack of correlation between λ_1 and any of the experimentally observed features of the infected cell (Fig. 4c and Supplementary note 11) suggests that viral genome replication and late genes transcription is independent of the host physiology, at least in these experimental settings. Surprisingly, we also observe a significant negative correlation between λ_1 and λ_2, suggesting the presence of a negative feedback between viral genome replication and translation. A possible explanation is that, if translation is fast, viral capsids might assemble rapidly, spooling in viral DNA and thus depleting the pool of viral genomes that could replicate. Further work is necessary to test this or alternative hypotheses.

Gradual perforation of the cell membrane precedes the abrupt lysis of the infected cell

The concluding stage of the infection process involves the lysis of the host cell. We collected high-frame rate images (100 Hz) to visualise the events preceding cell lysis (Methods, Supplementary movie 4). The process of lysis unfolds in two distinct phases. The initial phase, here termed as perforation, involves a gradual leakage of material from the cell, resulting in a subtle increase in phase brightness (Fig. 5b), accompanied by a gradual decrease in the intensity of the surrounding environment. This phase is slower, lasting several seconds, and typically begins with a small but sharp increase in phase brightness (Fig. 5d), marking the onset of perforation (t_4). Material is then steadily lost from the cell until the commencement of the second phase at t_5. The subsequent phase, referred to as lysis, represents the final structural breakdown of the cell envelope. This is indicated by the rapid increase in the phase contrast intensity (purple arrow in Fig. 5d). We estimated the mean duration between the onset of perforation and the start of lysis (t_4 to t_5) to be 6.57 s.

In Fig. 3d, we observe that in some infections, the YFP signal drops in the final observation prior to lysis. This phenomenon is only observed in a fraction of the infection events due to the short interval between perforation and lysis compared to the frame rate of the images taken. With a mean perforation to lysis time of 6.57 s, we only expect to observe the drop in YFP in 21.9% of infections when imaging at 2 frames min^{-1}, which is consistent with the results shown in Fig. 3d and the observed increase in phase contrast signal of those cells (indicating a loss of material from the cell) as shown in Fig. S7.

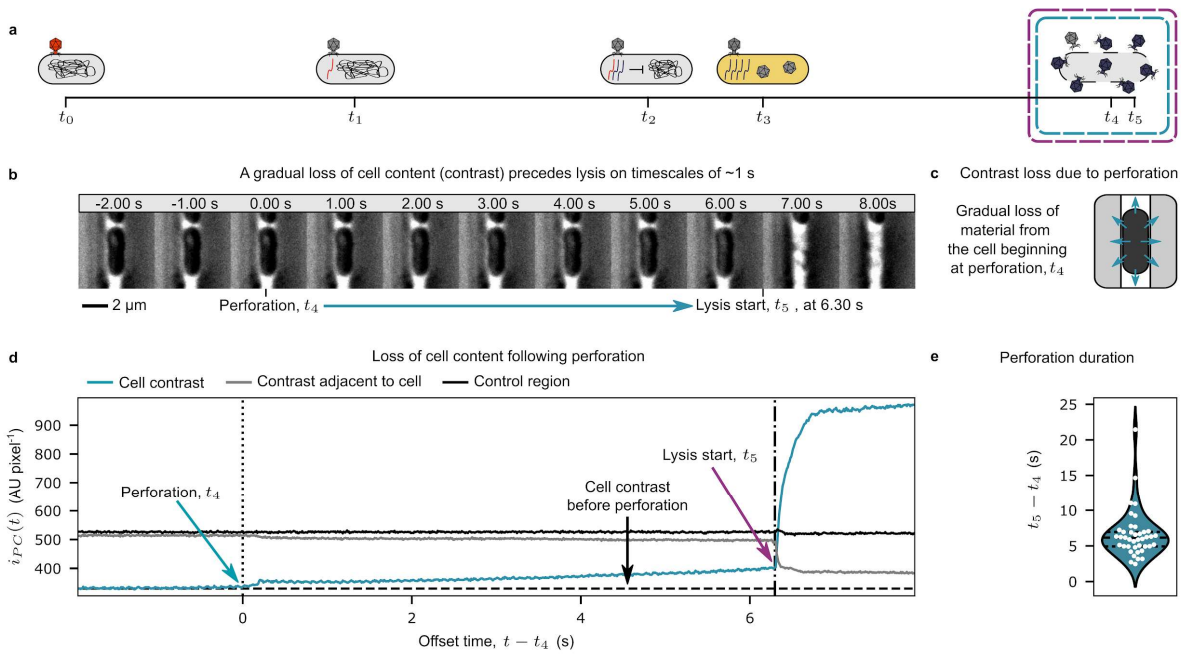

Fig. 5: A gradual loss of cell contents precedes cell lysis
a. A timeline of the T7 phage life cycle, indicating the timing of perforation (t_4) and lysis (t_5). **b.** A kymograph showing the cell lysis on timescales of 1.00 s. The time axis is offset such that perforation (t_4) starts at time zero. **c.** A schematic illustrating the gradual loss of material from the cell which follows perforation and gives a loss of contrast in the images. **d.** Time series data showing the phase contrast intensity within and outside the cell shown in the kymograph in (**b**). **e.** Violin plot showing the distribution of perforation duration across different infection events (perforation start to lysis start, t_4 to t_5). The mean perforation duration is 6.57 s (n = 41, CV = 51%).

Heterogeneity in lysis time is driven by variability in the early stages of infection

Having measured the timing of several points in the infection cycle, we set out to construct a full timeline of the typical T7 infection cycle, alongside a comparison of the relative contributions of each individual infection step to the overall variability in lysis time.

Fig. 6a illustrates a comprehensive timeline of the typical infection cycle of T7* on *E. coli* cells, from phage adsorption onto the cell to the mean of four key time points in the infection cycle: genome injection (t_1), host cell shutdown (t_2), capsid production (t_3), and cell lysis (t_5). Error bars accompany each time point, representing the range of variability (95% confidence interval). The perforation step (t_4) is not represented here due to its negligible duration compared to the other stages (Fig. 5).

Analysis of this timeline reveals that genome injection typically concludes 4.8 min after phage adsorption, accounting for just over one quarter of the overall lysis time (18.8 min). Approximately 9.2 min into the infection cycle, the host cell ceases growth, then capsid production starts at 11.1 min after adsorption. However, the adjusted production start time

inferred from the model ($t_3 *$) is 9.3 mins after adsorption, suggesting the capsid production actually starts almost simultaneously with host takeover. Approximately 9.6 min after the host takeover (calculated as $t_5 - t_2$), the cell undergoes lysis, releasing the phage copies into the surrounding environment. The average duration from adsorption to lysis, the lysis time, is 18.8 ± 1.6 min for T7*, consistent with the value obtained from bulk experiments (20.1 ± 2.7 min, n = 3, Fig. 6c, Supplementary note 12). For wild type T7 phage without the genomically integrated capsid expression reporter, we estimated the average time between adsorption and lysis to be 16.2 ± 0.9 min, also consistent with the corresponding bulk average (14.8 ± 1.9 min, n = 3, Fig. 6c). The observed difference in lysis time between the two strains could be explained by the additional burden imposed by the expression of the capsid reporter.

Our results show that the lysis time exhibits a CV of 21% across infection events. Fig. 6b illustrates the contribution of each step in the infection cycle towards this variability. Here, all time points are directly measured with reference to cell lysis, as this is the most sudden and clearly identifiable of the events. We find that the variability in the overall lysis time is comparable to the variability in the time interval between the end of injection (t_1) and lysis (t_5). Conversely, both the durations between growth arrest and lysis (t_2 to t_5), and capsid production start and lysis (t_3 and t_5), are very consistent, with interquartile ranges spanning just 1.5 min (<10% of the lysis time). These data suggest that the primary sources of variability in lysis time stem from the initial stages of infection up to the point in which cell growth stops. After this point, which delineates the time when the phage has likely taken control of the host cellular machinery, the timing of events is remarkably consistent across infection events.

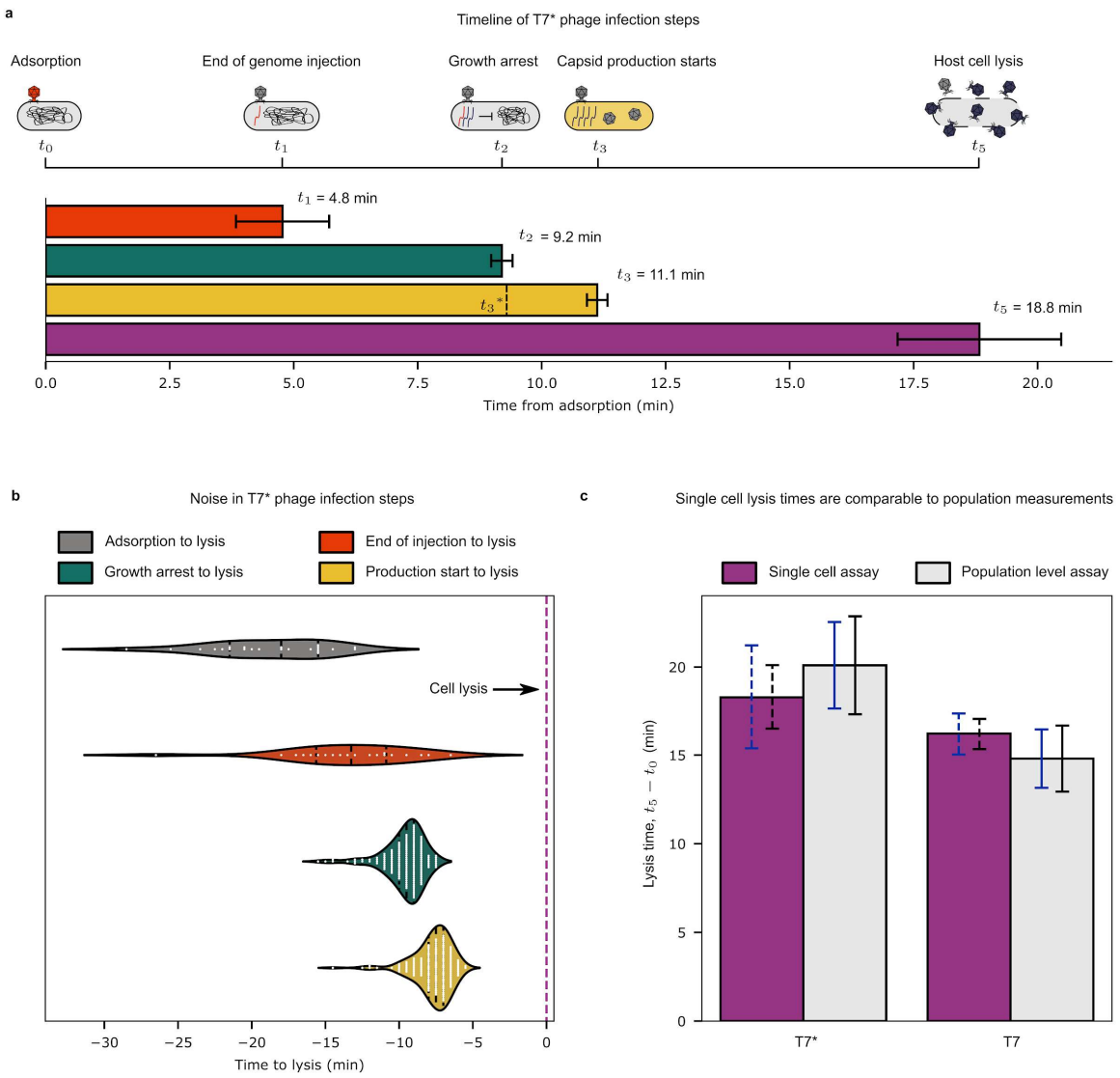

Fig. 6: The timing of individual steps of infection and the associated variability across events

a. Timeline of phage infection steps. Each bar represents the mean time from adsorption to the indicated time point in the T7* phage life cycle. The adjusted production start time from the model results in Fig. 4, $t_3 *$, is indicated as a dashed line on the yellow bar. The error bars represent a 95% confidence interval. The data is pooled from three single cell experiments, giving total sample sizes for the measurement of t_1 (injection end), t_2 (growth arrest), t_3 (production start) and t_5 (lysis) of 20, 166, 160 and 23, respectively. **b.** Kernel density estimates of the timing distributions from different time points in the T7* phage life cycle to lysis. Each single-cell infection event measured is shown as a white dot. Inner and outer dashed lines in each violin represent the median and lower and upper quartiles respectively. Adsorption to lysis (grey violin) has mean 18.8 min, CV = 21%, n = 23. Injection end to lysis (orange violin) has mean 13.4 min, CV = 33%, n = 20. Growth arrest to lysis (green violin) has mean 9.6 min, CV = 15%, n = 166. Production start to lysis (yellow violin) has mean 7.7 min, CV = 17%, n = 160. The perforation to lysis time is not included, as relative to the timescales of the other steps, the contributed noise from this step is negligible (the mean is 6.57 s, CV = 51%, n = 41). **c.** Lysis times measured with single-cell and population level methods are comparable. Purple bars represent the mean of single-cell lysis times from one experiment,

427 and grey bars represent the mean of three population level lysis time measurements (three
428 biological replicates). Accordingly, dashed error bars are calculated from single-cell data as
429 described, and solid error bars are calculated from biological replicates of population level
430 assays. The blue error bars represent ± 1 standard deviation, and the black error bars
431 represent the 95% confidence interval. The mean lysis times of T7* obtained from single-cell
432 and population level measurements (18.3 min, n = 10 and 20.1 min, n = 3 respectively) are
433 not significantly different when compared with a t-test. The mean lysis times of T7 obtained
434 from single-cell and population level measurements (16.2 min, n = 7 and 14.8 min, n = 3
435 respectively) are also not significantly different when compared with a t-test. For all data in
436 Fig. 6, events with a lysis time of 30 min or more are treated as outliers and excluded from the
437 distribution. More detail on the single-cell selection criteria is given in Supplementary note 13.

438 Lysis time variability can provide fitness advantages to phage 439 populations

440 Lysis time represents a key life history parameter for lytic phages and is known to be under
441 strong selective pressure in laboratory experiments[36–40] and potentially in the wild. Its fitness
442 effect on phage populations in different environments is theoretically well studied, however,
443 due to the lack of experimental data regarding its level of stochasticity, it is typically assumed
444 to be either noiseless or exponentially distributed for modelling convenience[41–44]. Our data
445 provide the unprecedented opportunity to quantify lysis time variability, raising the question of
446 whether it can represent an evolutionary trait conferring a fitness advantage to a phage
447 population.
448
449 To investigate this question, we used stochastic agent-based simulations of a serial passage
450 experiment, in which two phage populations, denoted as “wild type” and “mutant”, are initially
451 mixed in equal proportion and then passaged through several population bottlenecks until one
452 phage approaches fixation (Fig. 7a, Methods, Supplementary note 14). The wild type and
453 mutant phage share the same burst size distribution, but have distinct and inheritable lysis
454 time distributions. Some examples of these distributions are shown in Fig. 7c. Mutant 1 has
455 the same mean lysis time as the wild type, but different standard deviation. Mutant 2 has the
456 same mean and standard deviation in lysis time as the wild type, but different skew.
457
458 Fig. 7d shows the probability of mutant fixation as a function of standard deviation (mutant 1,
459 left panel) and skew (mutant 2, right panel) determined over 25 independent simulations. The
460 results show that a larger standard deviation confers a fitness advantage, if mean and skew
461 are the same, while a negative skew in lysis time is advantageous when the mean and
462 standard deviation are the same. Overall, our results clearly indicate that the mean lysis time
463 alone is not sufficient to predict phage fitness, and the higher order moments of the distribution
464 can significantly alter a phage’s competitive advantage. We note that, although here we
465 investigate the effect of variation in lysis time, while keeping the other phage life history
466 parameters constant, in reality, these parameters are likely dependent on each other, giving
467 rise to a range of tradeoffs. Future work will explore how such inter-dependencies in variability
468 can shape phage fitness.

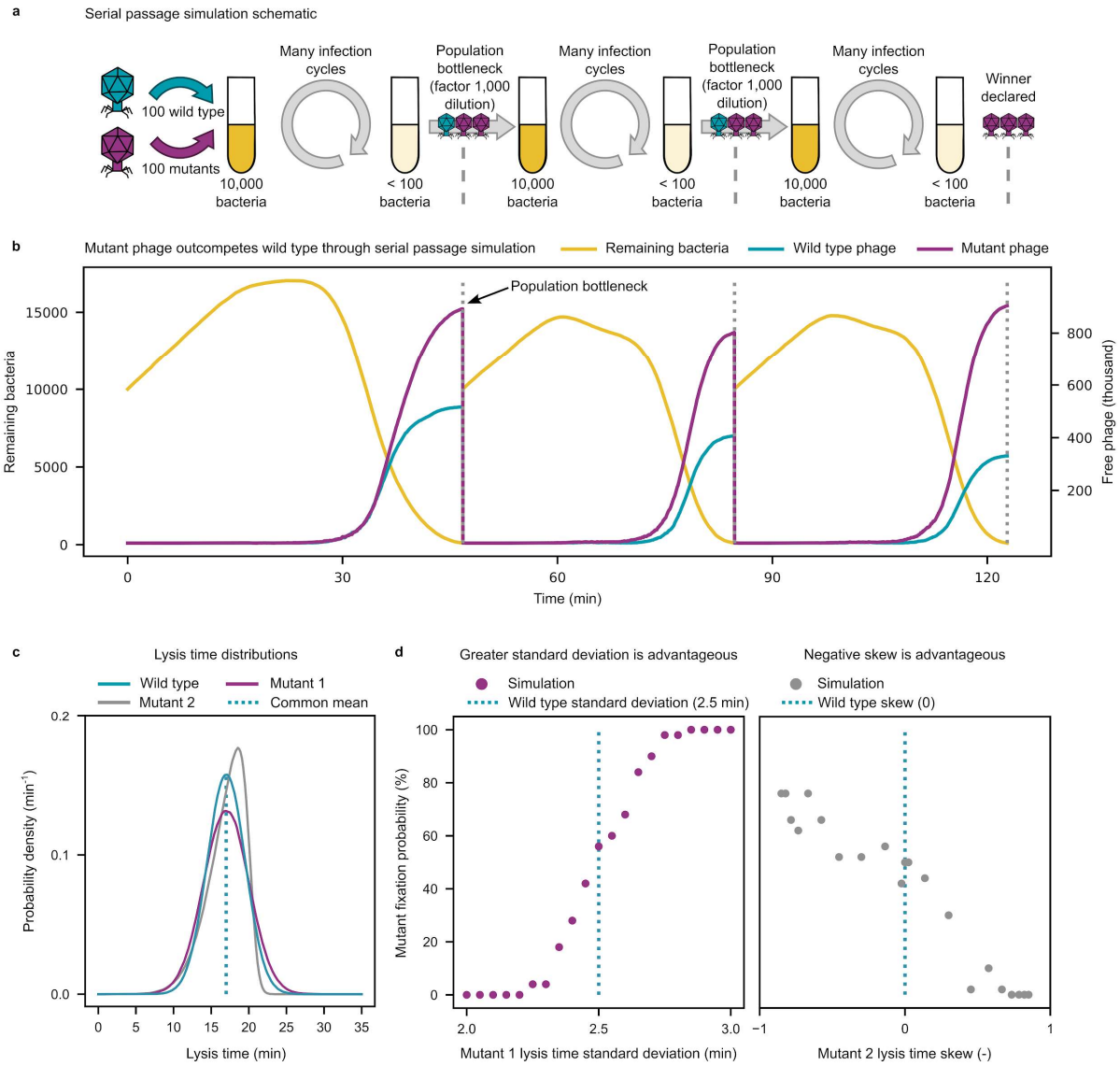

Fig. 7: Simulations predict lysis time variance and skewness impact phage fitness **a.** A schematic explaining the serial passage simulation, where a wild type and mutant phage with corresponding lysis times drawn from different distributions (Fig. 7c) compete and undergo several rounds of dilution into fresh bacteria (Methods, Supplementary note 14). **b.** Example time series data from the simulations, demonstrating the growth and lysis of the bacteria (yellow line), and the proliferation of the wild type and mutant phage (blue and purple lines respectively). At the population bottleneck, a 1000 fold dilution of the phage into fresh bacteria is simulated. If, after a bottleneck, one phage accounts for more than 70% of the total phage population, it is declared the winner. **c.** Example lysis time distributions of wild type and mutant phage. Mutant 1 (purple) has the same mean as the wild type (blue), but the standard deviation in lysis time is varied (Fig. 7d, left panel). Mutant 2 (grey) has the same mean and standard deviation as the wild type, but the skew in lysis time is varied (Fig. 7d, right panel). **d.** When competing against a wild type phage, mutants with lysis times drawn from a distribution with equal mean but greater variance are predicted to have a fitness advantage (left panel). Mutants with lysis times draw from a distribution with equal mean and variance to the wild type but with negative skew are also predicted to have a fitness advantage (right panel). Each data point is computed from 25 simulations.

Discussion

Here, we have reported the first study that quantifies the kinetics of individual steps in the lytic cycle of phage T7 at single phage-single cell resolution. Our novel assay provides a new way to quantify phage-bacteria interactions that is orthogonal to omics analyses, which provide dynamic but averaged phenotypes, and structural investigation, which assess variability but are based on static observations. Our approach enables dynamic measurements across many infection events in a precisely controlled environment, while maintaining the individuality of each of them in order to assess variability and correlations across the phenotypes of the phage and the corresponding infected cell.

We find that the major source of variability in the timing of infection events comes from the early steps of viral DNA entry up to cell growth arrest, while the second part of the infection process, between host take-over and cell lysis, is remarkably robust. A possible explanation for this difference is that the initial steps of infection rely on low copy-number molecules, such as one viral genome, or an initial few copies of T7 RNAP, which are subject to large relative number fluctuations. However, we cannot exclude that variability in the structural properties of the capsid[45] and consequent attachment to the host cell receptors might contribute to what we observe. Future studies that quantify the proportion of unsuccessful adsorptions on one side, and the spatial dynamic of the T7 RNAP within the infected cell, on the other, will help answer this question.

The second phase, in which capsid proteins and, arguably, viable phage particles are produced within the host cell, exhibits a surprisingly large variability in kinetics and final amount, despite the robustness in the timing of the events. The strong correlation between the total protein production and the size of the growth-arrested host suggests that this variability may originate in physiological differences across infected cells. Indeed, using our mathematical model, we find that the phage protein production rate strongly depends on the translational resources of the cell, which scale with cell size, providing a strong mechanistic link between host cell physiology and phage burst size.

Accurate quantification of the sources of phenotypic variability and their relative correlations across infection events is not only important to understand the underlying molecular mechanisms controlling phage infection outcomes, but can also have significant evolutionary consequences. Our simulation results clearly show that mean phenotypic values, such as average lysis time, are insufficient to predict the fitness advantage of a phage population and that higher moments of the distribution can have a significant impact. These findings open the intriguing and currently under-explored possibility that variability in phage phenotype could be under strong selective pressure[46,47], raising fascinating questions regarding how evolution shapes it in different scenarios.

Finally, although this work has primarily focused on T7-*E. coli* to benchmark the assay using a well-studied model system, the approach can readily be applied to any natural, evolved, or engineered phage. The high-throughput and scalable nature of the platform can be harnessed for multiplexity, to benchmark a variety of sequence variants of phages against specific target bacteria or multiple mutants of a target bacteria against a particular phage. Precise characterisation of properties associated with infection steps (such as adsorption, production,

533 and lysis) can generate a multi-phenotypic profile for each phage-bacteria pair, enabling
534 detailed analysis of mechanisms underlying response, resistance, and phage-bacteria co-
535 evolution. Similarly, a collection of natural or engineered phages can be evaluated for their
536 efficacy in eradicating a target strain, with implications for medical or biotechnological
537 applications. In summary, this assay promises to open up new avenues for the systems
538 analysis of phage-bacteria interactions and their practical applications.
539

Online Methods

Bacterial strains and growth conditions

The following bacterial strains were used in this study.

Table 1: List of *E. coli* strains used in this study

Name	Species	Genotype	Use
SB8	*E. coli*	MG1655 7740 Δ*motA*	Experiments for Figs. 1 to 6.
SB7	*E. coli*	SB8-*glmS*::PRNA1-mCherry-mKate2	Microfluidic device optimisation experiment (Supplementary note 3), training data for cell segmentation (Supplementary note 4).
BW25113	*E. coli*	BW25113	Generating phage lysates.

The motility knockout in SB8 and SB7 prevents cells leaving the trenches of the microfluidic device. Prior to experiments in the microfluidic device, cells were grown overnight in a shaking incubator at 250 rpm and 37 ºC in LB Miller (Invitrogen) containing 0.8 g L^{-1} of pluronic F-108 (Sigma-Aldrich, 542342). Cultures were started directly from a frozen stock to maintain a consistent genetic diversity across the cells used in experiments across different days. The LB Miller was sterilised by autoclaving. The pluronic F-108 was first prepared as a 100 g L^{-1} solution and filter sterilised, and then diluted 0.8 % v/v into the LB Miller.

Phage lysate preparation

E. coli BW25113 strain cells were grown overnight in a shaking incubator at 250 rpm and 37 ºC in LB Miller (Invitrogen). 500 µL of the overnight liquid culture was used to inoculate 20 mL volume of LB Miller and left to grow in a shaking incubator at 37 ºC for 1 h 40 min. Once the culture reached OD 0.6-0.7, 500 µL of stock phage lysate was added and left in the shaking incubator for 7 min. The phage-inoculated cells were centrifuged in a pre-chilled (4 ºC) centrifuge at 5000 rpm for 5 min. The supernatant was discarded and the pelleted cells were resuspended in 2 mL of fresh LB Miller. The resuspended culture was left in the shaking incubator for 1 h at 37 ºC for the infected cells to fully lyse. The lysate was transferred into 1.5 mL Eppendorf tubes and centrifuged at 14000 rpm for 10 min. The resulting supernatant was passed through 0.22 µm filters to remove any traces of cell debris and unlysed cells.

PFU estimation

The number of plaque forming units (PFU) in the filtered lysate was estimated using a plaque assay. For this, serial dilutions of the filtered lysate were set up ranging from dilution factor 10^5 to 10^8. 20 µL of each diluted lysate was mixed with 100 µL of overnight BW25113 cells in 5 mL of 0.7% agar LB, kept at 50 °C. The mixture was briefly vortexed and poured as a thin layer of agar on 9 cm-diameter plates and incubated at 37 °C for 4 h. The formed plaques

were counted and the number divided by 20 to estimate the number of PFU per μL of each dilution factor. Measurements across three dilution factors were used to estimate the concentration of PFUs per μL of the filtered lysate. The titres of lysates obtained using the above method are listed in Table 2. Filtered lysate was used either directly or stained as per protocol below. Note that lysate titres listed in Table 2 are diluted into growth media for microfluidic experiments.

Table 2: List of T7 strains and typical corresponding lysate PFUs obtained

Experiment	Phage strain	Lysate PFU
Figs. 1, 3, 6	T7*, Sytox Orange labelled	1.0×10^7 μL^{-1}
Fig. 2	Wild type (WT) T7, Sytox Orange labelled	3.5×10^7 μL^{-1}
Fig. 5	WT T7, unlabelled	4.0×10^7 μL^{-1}

Genetic engineering of phage: construction of T7*

Transgenic T7 strain T7* was created by assembling PCR-cloned fragments of WT T7 genome along with the fragment encoding T7 phi10 promoter followed by *E. coli* codon-optimised mVenus NB (SYFP2) into a circular plasmid. This circularised transgenic genome was then electroporated into BW25113 cells to produce the transgenic phage lysate. Virions from individual plaques were isolated and sequenced to establish the isogenic strain of T7*. A full description of the PCR protocol to clone the required fragments, the Gibson Assembly of the transgenic genome, the electroporation protocol and the isolation of transgenic strains is available in Supplementary note 1.

Staining the DNA of the phage genome

The phage lysate was treated with DNAse I-XT to remove any residual bacterial DNA and then stained with Sytox Orange at the final concentration of 25 uM. Details of the DNAse I-XT treatment and Sytox Orange staining protocol are available in Supplementary note 2.

Population level measurement of lysis time

Population level measurements of the mean lysis time of wild type T7 and T7* were carried out according to the 'one-step growth curve' or 'lysis curve' protocol[48], a full account of which is available as Supplementary note 12. Measurements were taken in LB using SB8 (Table 1) as the host bacteria. Each phage's lysis time was measured over three biological replicates, and we find these values to be 14.8 ± 1.3 min for wild type T7, and 20.1 ± 2.0 min for T7* (mean ± 1 standard error of the mean).

Microfluidic device fabrication

The microfluidic devices were fabricated using soft lithography, by casting a silicone elastomer onto a silicon wafer. We received this wafer as a gift from Dr. Matthew Cabeen of Oklahoma State University. It was fabricated by the Searle Clean Room at the University of Chicago (https://searle-cleanroom.uchicago.edu/) according to the specifications provided by Dr.

605 Cabeen and his colleague, Dr. Jin Park. These specifications were based on the design
606 presented by Norman *et al.*[21]. The silicone elastomer was prepared by mixing
607 polydimethylsiloxane (PDMS) and curing agent from the Sylgard 184 kit (Dow) in a 5:1 ratio
608 and degassing for 30 min in a vacuum chamber. The elastomer was then poured onto the
609 silicon wafer and degassed in a vacuum chamber for a further 1 h. The elastomer was then
610 cured for 1 h at 95 °C. The appropriate devices were then cut out and inlet and outlet holes
611 were punched with a 0.75 mm biopsy punch (WPI). Devices were then cleaned with Scotch
612 Magic tape before being sonicated in isopropanol for 30 min, blow dried with compressed air
613 and then sonicated in distilled water for 20 min. 22x50 mm glass coverslips (Fisherbrand) were
614 sonicated for 20 minutes in 1 M potassium hydroxide, rinsed and then sonicated for 20 min in
615 distilled water before blow drying with compressed air. The devices and coverslips were then
616 dried for 30 min at 95 °C. Devices and coverslips were plasma bonded using a Diener
617 Electronic Zepto plasma cleaner, by first pulling a vacuum to 0.1 mbar, and then powering on
618 the plasma generator at 35% and admitting atmospheric air to a chamber pressure of 0.7 mbar
619 for 2 min. Device and coverslip were then bonded and heated on a hotplate at 95 °C for 5 min,
620 before transferring to an oven at 95 °C for 1 h to produce the finished microfluidic devices.

621 Single cell infection assay

622 On the day of the experiment, sterile growth media containing LB Miller (Invitrogen) with 0.8 g
623 L^{-1} pluronic F-108 (Sigma-Aldrich) was loaded into a syringe. The pluronic is added as a
624 surfactant to prevent cell clumping in the overnight culture, to improve cell loading, and to
625 prevent cells clumping at the outlet of trenches. It is added to the media at sub-inhibitory
626 concentrations[15]. The lane of the microfluidic device to be loaded was first passivated by
627 adding the above described growth media into the lane with a gel loading tip, and allowing it
628 to rest for 10 min. A 1 mL volume of the cells grown overnight were transferred into a 1.5 mL
629 tube and spun gently at 1000 g for 3 min to sediment the cells. The supernatant was poured
630 away and the cells resuspended in the residual volume. A small volume of this dense cell
631 culture was then pushed into the passivated lane using a gel loading tip and left to rest for 10
632 min. During this time, the small stationary phase cells will diffuse into the trenches.
633
634 While the cells are diffusing into the trenches, growth media from the syringe is pushed through
635 a silicone tubing path to purge the tubing of air. The tubing has a forked path, and the flow is
636 directed down a given fork using a 3-way solenoid pinch valve (Cole Parmer). One fork
637 supplies the microfluidic device with growth media, while the other leads directly to the waste
638 bottle.
639
640 The media flow is then connected to the lane of the device containing the cells using 0.83 mm
641 outer diameter needles. The outlet flow goes to a waste bottle. Inlet flow from the media
642 syringe is driven by a syringe pump, and initial flow is set to 100 μL min^{-1} for 10 min to clear
643 excess cells from the lane. Media flow is then reduced to 5 μL min^{-1}. Following this, 365 nm
644 illumination light is shone onto the inlet of the device such that each part of the inlet receives
645 at least 7 min of illumination. This kills any cells not removed by the high flow rate, and helps
646 to prevent biofilm formation in the device inlet.
647
648 The cells are grown in the device for a minimum period of 3 h from the introduction of fresh
649 growth media into the lane, to allow the cells to reach a steady state, exponential growth
650 phase. After this wake up period, the media is switched to media containing phage to begin

651 the infection imaging. A typical phage media composition is described in Table 3, which would
652 result in a final phage titre of 10^6 PFU μL^{-1}. Note that the phage lysate is also washed and
653 resuspended in LB Miller (Supplementary note 2), so the exact lysate volume used is unlikely
654 to significantly change the nutritional composition of the media.
655
656 **Table 3: Phage treatment media composition**

Component	Volume (µL)	Volume fraction (-)	Concentration in media
LB Miller	4460	0.892	N/A
Pluronic F-108, 100 g L^{-1}	40	0.008	0.8 g L^{-1} pluronic F-108
Phage lysate, PFU 10^7 μL^{-1}	500	0.100	10^6 PFU μL^{-1}
Total	5000	1.000	N/A

657
658 The phage titre must be sufficiently high to ensure at least some infections occur in each given
659 trench, but the exact titre is unimportant in the ranges used, as we operate at very low
660 multiplicity of infection in order to ensure that all first round infections result from just one
661 phage binding to a cell. The phage titres used in each experiment are listed in Supplementary
662 table 6.
663
664 To change the media to phage media, the solenoid pinch valve is activated to block flow to
665 the microfluidic device. The flow to the microfluidic device is blocked for a maximum of 10 min.
666 While it is blocked, the growth media syringe is changed to a syringe containing growth media
667 with phage, and then the tubing is flushed with the phage media at high flow rates, such that
668 the growth media without phage is completely cleared from the tubing. Then, the flow rate is
669 returned to 5 µL min^{-1} and the flow is switched to introduce phage media to the cells. Purging
670 the initial section of tubing with phage media reduces the time between the switch and the
671 phages reaching the cells, without having to expose the cells to high flow rates which could
672 cause mechanical stress. Additionally, it purges bubbles which can sometimes be introduced
673 when the syringes are switched.
674
675 Once the media is switched, time-resolved image acquisition begins.

676 Time-resolved image acquisition

677 Images were acquired using a Nikon Eclipse Ti2 inverted microscope with a Hamamatsu
678 C14440-20UP camera. The microscope has an automated stage and a perfect focus system,
679 which automatically maintains focus over time. The microscope contains two multiband filter
680 cubes, each of which contains a multi-bandpass dichroic mirror and corresponding multiband
681 excitation and emission filters. There is an additional emission filter which can be quickly
682 switched to select the correct emission wavelength band. Together the multiband cubes and
683 the emission filter wheel allow for fast imaging in multiple colour channels. All captured images
684 are initially saved using Nikon's ND2 file format. For the experiments in Figs. 1, 2, 3 and 6,
685 imaging began before the phage media reached the cells, and continued at a regular
686 frequency for the duration of the experiments.

687
688 The microscope settings used for each channel are listed in Table 4 below.
689
690 **Table 4: Imaging settings for different experiments used in this paper**

Experiment	Channel	Light source	Filter cube	Emission filter band centre/ band width (nm)	Objective	Imaging interval (s)
Figs. 1, 3, 6	Yellow	514 nm	LED-CFP/YFP/mCherry-3X3M-A	540/21	Plan Apo λ 100x Oil Ph3 DM	30
Figs. 1, 3, 6	Orange	561 nm	LED-DA/FI/TR/Cy5-B	595/40	Plan Apo λ 100x Oil Ph3 DM	30
Figs. 1, 3, 6	Phase contrast	Köhler	LED-CFP/YFP/mCherry-3X3M-A	540/21	Plan Apo λ 100x Oil Ph3 DM	30
Fig. 2	Orange	561 nm	LED-DA/FI/TR/Cy5-B	595/40	Plan Apo λ 100x Oil Ph3 DM	10
Fig. 2	Phase contrast	Köhler	LED-DA/FI/TR/Cy5-B	515/30	Plan Apo λ 100x Oil Ph3 DM	10
Fig. 5	Phase contrast	Köhler	LED-DA/FI/TR/Cy5-B	515/30	Plan Apo λ 100x Oil Ph3 DM	0.01

691
692 We have used high-speed timelapse imaging (100 frames s^{-1}) to capture the events preceding
693 the lysis, as our initial attempts using 1 frame s^{-1} imaging revealed that the structural changes
694 occurring during lysis unfold on sub-second timescales. The high frame rate, while conducive
695 to observing rapid dynamics, renders fluorescence imaging unsuitable due to photobleaching
696 and potential phototoxicity. Nonetheless, phase-contrast imaging is sufficient to gain a detailed
697 insight into the material loss from the cell to its surroundings in the fleeting moments preceding
698 lysis (Fig. 5). A short exposure time (3 ms) and a small region of interest (ROI) around
699 individual trenches enabled us to achieve an imaging interval of 10.2 ms (Supplementary
700 movie 4).

701 Image preprocessing

702 All captured images were pre-processed before feature extraction. First, individual frames
703 from the Nikon ND2 format were extracted and saved as PNG files using custom Python code
704 which makes use of the nd2 module (https://pypi.org/project/nd2/). Using custom Python code
705 (https://github.com/georgeoshardo/PyMMM), these frames were then registered to correct for

706 any stage drift and rotated to ensure the trenches were vertical in the images. We then use
707 automated methods to find the position of each trench in the images and crop out the trenches
708 for further processing, as described below.

709 Cell segmentation

710 The phase contrast images of cells in the extracted trench images from our experiments in
711 Figs. 1, 3 and 6 were segmented using a custom trained Omnipose machine learning model[49].
712 The model was trained on images (taken on a different day) of SB7 *E. coli* (Table 1) growing
713 in our device where both fluorescence and phase contrast images were acquired using the
714 same objective as for the experiments. These images will be referred to as training images,
715 and are separate from the experiment image data.
716
717 To train the model, our approach was to first train an Omnipose model to segment
718 fluorescence images. To generate a high volume of training data and corresponding ground
719 truth masks for fluorescence images of cells in the mother machine, we use a virtual
720 microscopy platform called SyMBac[23]. Using this fluorescence model, we segmented
721 fluorescence images of cells and generated cell masks for the fluorescence channel of the
722 training images.
723
724 The cell masks for the fluorescence channel were then checked against the phase contrast
725 training images, and pairs of fluorescence masks and phase contrast training images which
726 matched well were manually curated into a training data set. This training data was used to
727 train an Omnipose model for the segmentation of phase contrast images. The phase contrast
728 model was then used to generate cell masks for the experiment image data. This pipeline is
729 further described in Supplementary note 4.

730 Feature extraction

731 Basic cell properties, such as cell position, length, area, and YFP intensity, were extracted
732 from regions of the images corresponding to the cell masks produced by segmentation. The
733 cell properties were extracted using custom Python code
734 (https://github.com/CharlieW313/MM_regionprops) utilising the scikit-image regionprops
735 function[50]. For the data in Fig. 3, further properties are calculated from the basic cell properties.
736 Mathematical descriptions are found in Supplementary table 7 of Supplementary note 16.

737 Single cell lineage tracking

738 The single cell growth and lysis traces were tracked over time using features extracted at each
739 frame, including cell position, area, orientation, and Zernike moments. This process was done
740 using a custom Python script (https://github.com/erezli/MMLineageTracking). The algorithm
741 predicts many potential states of these features for each cell at subsequent time steps. It then
742 finds the best match to the feature states in the following frame to determine the tracking
743 outcome. The results are stored in tree-structured Python objects containing detailed cell
744 properties such as YFP mean intensity. The tracking results are manually checked by
745 visualising them in kymographs. Further information about the algorithm can be found in
746 Supplementary note 5.

Single phage tracking

To track the injection of the phage genome, we monitored the intensity of the bright spot indicating the phage location over consecutive frames until injection was complete. Spot intensity was measured as the mean intensity of a fraction of the brightest pixels in a rectangular box centred on the spot, with a control box alongside for background comparison. Genome injection duration was estimated as the time between adsorption and spot intensity returning to control box levels. Further details concerning the tracking of individual phage spots and the calculation of genome injection time are presented in Supplementary note 7.

Analysis of capsid production data

The fluorescence intensity in the yellow channel was analysed to determine the start of capsid production, as the time point where the signal from the YFP reporter of capsid production increases above the baseline. We subtract the background intensity from the raw total intensity of the YFP reporter to give a total intensity, $I(t)$, as described in Supplementary table 7. The production start time, t_3, is calculated as the first time point when the total intensity reaches a threshold value (chosen to be 1420 AU based on inspection of the intensity time-series), and then subsequently remains above that threshold for a total of four consecutive time points. This start is later adjusted to t_3* by fitting the model, as explained in Supplementary note 11.

Analysis of perforation and lysis

For the high time resolution imaging of phage induced lysis, a machine learning based approach for cell segmentation was unsuitable. This was because we wished to monitor the phase contrast intensity of the cell before, during and after lysis, so any attempt to segment the cells using features of the image would begin to fail as those features markedly changed through the lysis process. We therefore used a hand-drawn manual segmentation of a static region at the location of each cell in Fiji (ImageJ), as the cells did not move significantly over the short timescales of lysis. The mean phase contrast pixel intensity of this region, $i_{PC}(t)$, was then measured in each frame. By translating the static region by 1.43 μm to the left and right of the cell (along the short axis of the trench), the phase contrast intensities of the regions adjacent to the cell were also measured. By further translating the region on the right of the cell an additional 0.72 μm to the right and 4.29 μm along the long axis of the trench towards its closed end, a region in the side trench far away from the lysis was used as a control region for the phase contrast intensity.

To determine the start of perforation (t_4), the mean and standard deviation of the phase contrast intensity over 200 time points (a window ending a few seconds prior to the perforation start) were computed. The perforation start was declared when the phase contrast intensity first exceeds this calculated mean plus three standard deviations, for a minimum of five consecutive time points. The start of lysis (t_5) was determined as the point where the phase contrast intensity sharply increases from the perforation line (indicated by the arrow in Fig. 5d). We refer to the time interval between these two timepoints as the perforation time.

Serial passage simulations

The simulation extends infection kinetic ODEs[41] to a stochastic, agent-based model (for a full description of the implementation see Supplementary note 14). The simulation begins with 2 pools of 100 phage and 10,000 susceptible bacteria in a simulated well mixed volume of 10^{-5} ml. All bacteria begin the simulation in the 'uninfected' state, at random points in their cell cycle. In each simulation time-step, 'bacterial growth', 'adsorption', 'infection', 'lysis', and 'decay' substeps occur.

Once the number of cells has dropped below 100, we simulate a 'bottleneck': a 1,000 fold dilution of the phage and remaining cells, and addition of 10,000 new susceptible bacteria. The simulation continues, with bottlenecks occurring every time the bacterial population falls below 100, until either one phage pool outnumbers the other 70:30 and is declared the winner, or until a preset timeout, at which point we declare a tie.

Acknowledgements

We are thankful to the members of the Bakshi Lab and Fusco lab for their support and feedback on this work.

Declarations

Funding

The research in the Bakshi lab was supported by the Wellcome Trust Award (grant number RG89305), a University Startup Award for Lectureship in Synthetic Biology (grant number NKXY ISSF3/46), an EPSRC New Investigator Award (EP/W032813/1) and a seed fund from the School of Technology at University of Cambridge. The research in the Fusco lab was supported by the Department of Physics, University of Cambridge, a Royal Society Research Grant (RGS\R2\212131) and an ERC Starting Grant/UKRI Horizon Europe Guarantee (EP/Y030141/1). Charlie Wedd was supported by the UK Engineering and Physical Sciences Research Council (EPSRC) grant EP/S023046/1 for the EPSRC Centre for Doctoral Training in Sensor Technologies for a Healthy and Sustainable Future. Georgeos Hardo was supported by United Kingdom Biotechnology and Biological Sciences (BBSRC) University of Cambridge Doctoral Training Partnership 2 (BB/M011194/1). Michael Hunter was supported by a UKRI EPSRC Doctoral Studentship from the Department of Physics, University of Cambridge (2125180). Simulations in this work were performed using resources provided by the Cambridge Service for Data Driven Discovery (CSD3) operated by the University of Cambridge Research Computing Service (www.csd3.cam.ac.uk), provided by Dell EMC and Intel using Tier-2 funding from the Engineering and Physical Sciences Research Council (capital grant EP/T022159/1), and DiRAC funding from the Science and Technology Facilities Council (www.dirac.ac.uk).

Competing interests

The authors declare no competing interests.

Authors' contributions

S.B. and D.F conceived the study and were in charge of the overall direction and planning. C.W., T.Y., A.S., M.H., D.F., and S.B. designed the experiments and simulations. C.W. carried out the microfluidics microscopy experiments, A.S. and M.H. carried out the bulk experiments, and T.Y. carried out the staining and genetic engineering of phages. C.W., R.L., G.H., and S.B designed the data analysis pipeline and carried out the data analysis. M.H., A.S., and D.F. carried out the simulations and associated analysis. D.F. developed the mathematical model and associated analysis. C.W., D.F., and S.B., lead the manuscript writing. R.M. contributed experimental material and methods. All the other authors provided critical feedback and contributed to the manuscript.

Data availability:

Data for this paper is available from the Zenodo repository associated with this paper, which can be found at 10.5281/zenodo.13227935.

Code availability:

Microscopy images were registered using the custom-built python script: https://github.com/georgeoshardo/PyMMM. Registered images were segmented using an Omnipose model trained with synthetic image data generated using the SyMBac pipeline: https://github.com/georgeoshardo/SyMBac. Single-cell features from the segmented images were extracted using https://github.com/CharlieW313/MM_regionprop. The custom-built Python script for tracking individual cell lineages in time series data is available at: https://github.com/erezli/MMLineageTracking. Python scripts for phage diffusion simulations, phage competition simulations, and Matlab script for fitting gene-expression data to mathematical models are available at: https://github.com/FuscoLab/single-cell-phage-tracking .

References

1. Campbell, A. The future of bacteriophage biology. *Nat. Rev. Genet.* **4**, 471–477 (2003).
2. Koskella, B., Hernandez, C. A. & Wheatley, R. M. Understanding the Impacts of Bacteriophage Viruses: From Laboratory Evolution to Natural Ecosystems. *Annu. Rev. Virol.* **9**, 57–78 (2022).
3. Schwartz, M. The adsorption of coliphage lambda to its host: Effect of variations in the surface density of receptor and in phage-receptor affinity. *J. Mol. Biol.* **103**, 521–536 (1976).
4. Weigel, C. & Seitz, H. Bacteriophage replication modules. *FEMS Microbiol. Rev.* **30**, 321–381 (2006).
5. You, L., Suthers, P. F. & Yin, J. Effects of Escherichia coli Physiology on Growth of Phage T7 In Vivo and In Silico. *J. Bacteriol.* **184**, 1888–1894 (2002).
6. Davis, K. M. & Isberg, R. R. Defining heterogeneity within bacterial populations via single cell approaches. *BioEssays* **38**, 782–790 (2016).
7. Hyman, P. & Abedon, S. T. Practical Methods for Determining Phage Growth Parameters. in *Bacteriophages: Methods and Protocols, Volume 1: Isolation, Characterization, and Interactions* (eds. Clokie, M. R. J. & Kropinski, A. M.) 175–202 (Humana Press, Totowa, NJ, 2009).
8. Kobiler, O. *et al.* Quantitative kinetic analysis of the bacteriophage λ genetic network. *Proc. Natl. Acad. Sci.* **102**, 4470–4475 (2005).
9. Wolfram-Schauerte, M., Pozhydaieva, N., Viering, M., Glatter, T. & Höfer, K. Integrated Omics Reveal Time-Resolved Insights into T4 Phage Infection of E. coli on Proteome and Transcriptome Levels. *Viruses* **14**, 2502 (2022).
10. Conners, R. *et al.* Cryo-electron microscopy of the f1 filamentous phage reveals insights into viral infection and assembly. *Nat. Commun.* **14**, 2724 (2023).
11. Wang, C., Tu, J., Liu, J. & Molineux, I. J. Structural dynamics of bacteriophage P22 infection initiation revealed by cryo-electron tomography. *Nat. Microbiol.* **4**, 1049–1056 (2019).

876 12. Golding, I. Single-Cell Studies of Phage λ: Hidden Treasures Under Occam's Rug.
877 *Annu. Rev. Virol.* **3**, 453–472 (2016).
878 13. Kiss, B. *et al.* Imaging the Infection Cycle of T7 at the Single Virion Level. *Int. J. Mol.*
879 *Sci.* **23**, 11252 (2022).
880 14. Attrill, E. L., Łapińska, U., Westra, E. R., Harding, S. V. & Pagliara, S. Slow growing
881 bacteria survive bacteriophage in isolation. *ISME Commun.* **3**, 1–9 (2023).
882 15. Bakshi, S. *et al.* Tracking bacterial lineages in complex and dynamic environments with
883 applications for growth control and persistence. *Nat. Microbiol.* **6**, 783–791 (2021).
884 16. Jack, B. R., Boutz, D. R., Paff, M. L., Smith, B. L. & Wilke, C. O. Transcript degradation
885 and codon usage regulate gene expression in a lytic phage. *Virus Evol.* **5**, vez055 (2019).
886 17. Balleza, E., Kim, J. M. & Cluzel, P. Systematic characterization of maturation time of
887 fluorescent proteins in living cells. *Nat. Methods* **15**, 47–51 (2018).
888 18. Studier, F. W. The genetics and physiology of bacteriophage T7. *Virology* **39**, 562–574
889 (1969).
890 19. Van Valen, D. *et al.* A Single-Molecule Hershey-Chase Experiment. *Curr. Biol.* **22**,
891 1339–1343 (2012).
892 20. Bakshi, S. *et al.* Nonperturbative Imaging of Nucleoid Morphology in Live Bacterial
893 Cells during an Antimicrobial Peptide Attack. *Appl. Environ. Microbiol.* **80**, 4977–4986
894 (2014).
895 21. Norman, T. M., Lord, N. D., Paulsson, J. & Losick, R. Memory and modularity in cell-
896 fate decision making. *Nature* **503**, 481–486 (2013).
897 22. Wang, P. *et al.* Robust growth of Escherichia coli. *Curr. Biol. CB* **20**, 1099–1103 (2010).
898 23. Hardo, G., Noka, M. & Bakshi, S. Synthetic Micrographs of Bacteria (SyMBac) allows
899 accurate segmentation of bacterial cells using deep neural networks. *BMC Biol.* **20**, 263
900 (2022).
901 24. Chen, W. *et al.* Structural changes in bacteriophage T7 upon receptor-induced genome
902 ejection. *Proc. Natl. Acad. Sci.* **118**, e2102003118 (2021).
903 25. Swanson, N. A. *et al.* Cryo-EM structure of the periplasmic tunnel of T7 DNA-

904 ejectosome at 2.7 Å resolution. *Mol. Cell* **81**, 3145-3159.e7 (2021).
905 26. Pao, C.-C. & Speyer, J. F. Order of Injection of T7 Bacteriophage DNA. *J. Virol.* **11**,
906 1024–1026 (1973).
907 27. Molineux, I. J. No syringes please, ejection of phage T7 DNA from the virion is enzyme
908 driven. *Mol. Microbiol.* **40**, 1–8 (2001).
909 28. Kemp, P., Gupta, M. & Molineux, I. J. Bacteriophage T7 DNA ejection into cells is
910 initiated by an enzyme-like mechanism. *Mol. Microbiol.* **53**, 1251–1265 (2004).
911 29. García, L. R. & Molineux, I. J. Rate of translocation of bacteriophage T7 DNA across
912 the membranes of Escherichia coli. *J. Bacteriol.* **177**, 4066–4076 (1995).
913 30. Proshkin, S., Rahmouni, A. R., Mironov, A. & Nudler, E. Cooperation between
914 translating ribosomes and RNA polymerase in transcription elongation. *Science* **328**, 504–
915 508 (2010).
916 31. Kiro, R. *et al.* Gene product 0.4 increases bacteriophage T7 competitiveness by
917 inhibiting host cell division. *Proc. Natl. Acad. Sci.* **110**, 19549–19554 (2013).
918 32. Molshanski-Mor, S. *et al.* Revealing bacterial targets of growth inhibitors encoded by
919 bacteriophage T7. *Proc. Natl. Acad. Sci. U. S. A.* **111**, 18715–18720 (2014).
920 33. Doermann, A. H. The intracellular growth of bacteriophages. I. Liberation of
921 intracellular bacteriophage T4 by premature lysis with another phage or with cyanide. *J.*
922 *Gen. Physiol.* **35**, 645–656 (1952).
923 34. Abedon, S. T., Herschler, T. D. & Stopar, D. Bacteriophage Latent-Period Evolution as
924 a Response to Resource Availability. *Appl. Environ. Microbiol.* **67**, 4233–4241 (2001).
925 35. Wang, I.-N. Lysis timing and bacteriophage fitness. *Genetics* **172**, 17–26 (2006).
926 36. Nguyen, H. M. & Kang, C. Lysis Delay and Burst Shrinkage of Coliphage T7 by
927 Deletion of Terminator Tφ Reversed by Deletion of Early Genes. *J. Virol.* **88**, 2107–2115
928 (2014).
929 37. Bull, J. J. & Wang, I. -N. Optimality models in the age of experimental evolution and
930 genomics. *J. Evol. Biol.* **23**, 1820–1838 (2010).
931 38. Kerr, B., Neuhauser, C., Bohannan, B. J. M. & Dean, A. M. Local migration promotes

932 competitive restraint in a host-pathogen 'tragedy of the commons'. *Nature* **442**, 75–78
933 (2006).
934 39. Heineman, R. H., Bull, J. J. & Hansen, T. Testing Optimality with Experimental
935 Evolution: Lysis Time in a Bacteriophage. *Evol. Int. J. Org. Evol.* **61**, 1695–1709 (2007).
936 40. Kannoly, S., Singh, A. & Dennehy, J. J. An Optimal Lysis Time Maximizes
937 Bacteriophage Fitness in Quasi-Continuous Culture. *mBio* **13**, e03593-21 (2022).
938 41. Yin, J. & McCaskill, J. S. Replication of viruses in a growing plaque: a reaction-diffusion
939 model. *Biophys. J.* **61**, 1540–1549 (1992).
940 42. Fort, J. & Méndez, V. Time-Delayed Spread of Viruses in Growing Plaques. *Phys. Rev.*
941 *Lett.* **89**, 178101 (2002).
942 43. Hunter, M. & Fusco, D. Superinfection exclusion: A viral strategy with short-term
943 benefits and long-term drawbacks. *PLOS Comput. Biol.* **18**, e1010125 (2022).
944 44. Hunter, M., Krishnan, N., Liu, T., Möbius, W. & Fusco, D. Virus-Host Interactions
945 Shape Viral Dispersal Giving Rise to Distinct Classes of Traveling Waves in Spatial
946 Expansions. *Phys. Rev. X* **11**, 021066 (2021).
947 45. Coshic, K., Maffeo, C., Winogradoff, D. & Aksimentiev, A. The structure and physical
948 properties of a packaged bacteriophage particle. *Nature* **627**, 905–914 (2024).
949 46. Bull, J. J., Heineman, R. H. & Wilke, C. O. The Phenotype-Fitness Map in Experimental
950 Evolution of Phages. *PLOS ONE* **6**, e27796 (2011).
951 47. Dominguez-Mirazo, M., Harris, J. D., Demory, D. & Weitz, J. S. Accounting for cellular-
952 level variation in lysis: implications for virus–host dynamics. *mBio* **0**, e01376-24 (2024).
953 48. Ellis, E. L. & Delbrück, M. The Growth of Bacteriophage. *J. Gen. Physiol.* **22**, 365–384
954 (1939).
955 49. Cutler, K. J. *et al.* Omnipose: a high-precision morphology-independent solution for
956 bacterial cell segmentation. *Nat. Methods* **19**, 1438–1448 (2022).
957 50. Walt, S. van der *et al.* scikit-image: image processing in Python. *PeerJ* **2**, e453 (2014).
958 51. Pedro Coelho, L. Mahotas: Open source software for scriptable computer vision. *J.*
959 *Open Res. Softw.* **1**, 1–7 (2013).

960 52. Taheri-Araghi, S. *et al.* Cell-size control and homeostasis in bacteria. *Curr. Biol. CB*
961 **25**, 385–391 (2015).
962 53. Tinevez, J.-Y. *et al.* TrackMate: An open and extensible platform for single-particle
963 tracking. *Methods* **115**, 80–90 (2017).
964 54. Crocker, J. C. & Grier, D. G. Methods of Digital Video Microscopy for Colloidal Studies.
965 *J. Colloid Interface Sci.* **179**, 298–310 (1996).
966 55. Dunn, J. J. & Studier, F. W. Complete nucleotide sequence of bacteriophage T7 DNA
967 and the locations of T7 genetic elements. *J. Mol. Biol.* **166**, 477–535 (1983).
968 56. Steinier, Jean., Termonia, Yves. & Deltour, Jules. Smoothing and differentiation of data
969 by simplified least square procedure. *Anal. Chem.* **44**, 1906–1909 (1972).
970